Chapter 1

Introduction

At least one planet is orbiting every star (Batalha et al. 2013). Planets are formed within the accretion disk that is an important part of star formation. Most of the stellar mass is transported and processed by the disk while the left-over gas and dust become the building blocks of the planetary system. The processing within the disk alters the chemical structure of the gas and dust during the formation and evolution of disks up to their dissipation. While these two stages (formation and dissipation) are crucial, they are not well understood. One of the big questions in astronomy is how these changes in the physical and chemical structure during the early stages of star formation affect the planet formation process and the emergence of life.

The majority of chemical elements essential for life (SPONCH) as we know it are produced inside the stars. In the early universe, only chemical elements up to Lithium are synthesized (Galli & Palla 2013). The life-cycle of stars enriches the interstellar medium (ISM) by fusing elements to produce heavier elements up to iron (Fe) in the core through nuclear burning. The mass of the element that is synthesized in the stellar core is related to the mass of the star: only the more massive stars can produce Fe in their cores. Over time, more of these heavier elements are produced and incorporated into the next generation(s) of star and planet formation. These elements are then integrated into molecules, both simple and complex, during the star and planet formation process.

Star and planet formation are intimately linked through the disk. Disks have been proposed by Kant and Laplace in the 18^{th} century. Yet, it took another 2 centuries for the direct observational evidence of disks. The formation and evolution of disks dictate the amount of material delivered onto the star and of that what remains to form planets. This thesis focuses on the physical and chemical processes in the early stages of disk formation and evolution.

1.1 Star and planet formation

Stars form out of cold ($\sim 10 - 20$ K) dense molecular clouds (Bergin & Tafalla 2007) composed mostly of H_2 gas with 1% by mass in dust (Tielens 2005). With recent high sensitivity observations using the *Herschel Space Observatory*, it is known that these molecular clouds and star formation are located along filaments (André et al. 2010; Kennicutt & Evans 2012). Within these filaments, there are a variety of sizes and masses of molecular clouds. The more massive of these, especially at the point where filaments merge, will form star clusters (Schneider et al. 2012). There are small dense cores (≤ 0.1 pc, $n \sim 10^4$–10^5 cm^{-3}) along the filament which will form low-mass stars such as our Sun. Significant progress has been made recently in understanding the formation of these filaments and molecular clouds within them (Hennebelle & Falgarone 2012; André et al. 2014). Supersonic turbulence in the ISM causes the gas to compress into sheets and filaments. As a molecular cloud accumulates mass, gravity starts to become the dominant force and the cloud collapses to form cores that will form each individual star. In

addition, magnetic fields also control the flow of material on different physical scales.

The central protostar is a hot luminous ball of gas powered by the energy released by accretion in the protostellar phase and by nuclear reactions in its center at later stages. The stages of low-mass star formation ($M \leq 2\ M_{\odot}$) are relatively well understood compared to their higher mass counterparts but still several aspects remain unclear. While massive stars are luminous and easier to observe, low mass stars are more common. The study of the physical processes that take place during their formation provides insight into how our planetary system formed and on the emergence of life on Earth.

As the collapse proceeds, some material forms a disk as a consequence of energy and momentum conservation. Theoretical studies of disk properties did not start until the 1970s (Shakura & Sunyaev 1973). Early indirect evidence of disks has been found through optical polarization and spectra (Hartmann & Kenyon 1985, 1987) and mm-wave velocity fields (Sargent & Beckwith 1987). However, it is not until Strom et al. (1989) that the first statistical studies of disks emerged through the characterization of their spectral energy distributions (SEDs), thanks to the *Infrared Astronomical Satellite (IRAS)*. A follow-up survey of millimeter continuum emission by Beckwith et al. (1990) provided early mass estimates of disks around young stars. The key evidence was the first direct image of disks in 1994 using the *Hubble Space Telescope* (O'Dell & Wen 1994). Now, it is known that an accretion disk is present around every young star and it is a crucial part of star and planet formation (see Dullemond & Monnier 2010, Williams & Cieza 2011 and Luhman 2012 for recent reviews). This disk is usually called a circumstellar or protoplanetary disk (see Evans et al. 2009a for nomenclature). During the early stages of its evolution, the disk contains substantial amounts of gas, which is essential for the formation of gas-rich giants such as Jupiter.

Within these disks, planets eventually will form. Currently, there are over 1000 confirmed planets around other stars and more than 3000 candidates[1]. The current favorite scenario is that these planets are formed through coagulation of small dust particles to form larger bodies (Safronov 1969; Hayashi 1981; Pollack et al. 1996). It is expected that larger grains (>cm radius) move at larger velocities with respect to the gas. The drift velocity is maximal for 1 meter size bodies. At such velocities, the dust can either collide and fragment or drift inward onto the star before they grow to planetesimal size. This theoretical problem in planet formation is called the meter-size barrier. One possible solution is that these grains are covered by ices as proposed by Eddington (1937) and, finally, detected by Gillett & Forrest (1973). Over recent years following many surveys using ground-based telescopes and space observatories, it is clear that water is the main constituent of these ices as molecules freeze out and form on cold dust grains (e.g., Gibb et al. 2004; Öberg et al. 2011). The growth of particles may well be enhanced in regions of the circumstellar disk where these ices remain on the dust grains (Stevenson & Lunine 1988; Ros & Johansen 2013). The main difference between the mechanisms proposed by Safronov (1969) and the Kyoto model (Hayashi 1981) is that the latter focuses on the importance of gas dynamics.

To illustrate the stages of star formation leading toward planet formation, it is simplest to present the general sequence of the formation of an isolated low-mass star (see Figure 1.1). Isolated here means that it is formed out of a gravitationally collapsing spherical ball of gas and dust without the presence of any stars near enough such that they provide disturbances. The general sequence of star formation can be split into four 'Stages' that describe the transfer of mass from the large-scale envelope ($M_{\rm env}$) to the star ($M_{\star}$) (Robitaille et al. 2006; Dunham et al. 2014).

[1] see exoplanets.org for updated values

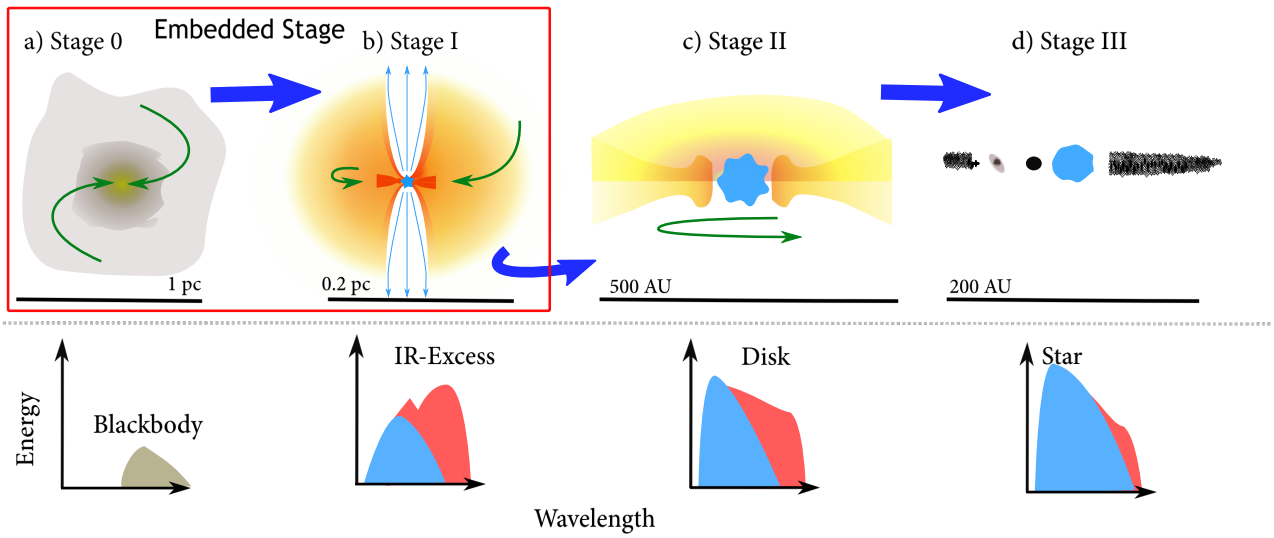

Figure 1.1 — *Top:* A sketch of low-mass star and planet formation. *a*: The embedded stage is indicated by the red box. Gravitational contraction occurs during Stage 0 on scales of 1 pc. *b*: A rotationally supported disk is present by Stage I embedded inside an envelope up to 0.1 pc. Jets and winds (thin blue arrows) launched from the inner regions create bipolar outflows and carve out a cavity. *c*: The envelope has dissipated away by Stage II and a $\sim$ 200 AU radius disk surrounds the pre-main sequence star (blue object). *d*: A planetary system has formed by Stage III. *Bottom:* Spectral energy distribution (SED) at each stage of evolution (energy as a function of wavelength increasing to the right). The different colors highlight the different components: the cold envelope is indicated by the brown color (*far left*), the warm disk/envelope emission is the red color, and the star is depicted by the blue color.

- **Stage 0** – Envelope mass is much greater than the central or protostellar mass ($M_{\rm env} \gg M_\star$). The dust thermal emission during this stage indicates a cold outer envelope. Highly collimated bipolar outflows are typically observed toward such objects (e.g., Bachiller & Tafalla 1999; Arce et al. 2007). This phase proceeds for $\sim 10^5$ years.
- **Stage I** – The central protostellar mass is greater than the envelope mass ($M_\star > M_{\rm env}$). The star and a possible disk contribution to the thermal emission is visible indicating a warm dust component. A weaker outflow component is typically associated with sources in this stage. The phase lasts $\sim 10^{5-6}$ years.
- **Stage II** – The envelope is largely dispersed and the central star is surrounded by a circumstellar disk. The sources in this stage are called classical T-Tauri stars. The emission at short wavelengths is dominated by the central protostar while the disk dominates the emission at longer wavelengths. The phase lasts $\sim 10^{6-7}$ years.
- **Stage III** – At this stage, the protostar is surrounded by a gas poor circumstellar disk (debris disk, see Wyatt 2008 and Matthews et al. 2014 for recent reviews). Planet(s) and asteroid belts must already be formed by this stage.

Stages 0 and I represent the embedded phase of star formation where a substantial mass still resides within the large-scale envelope as depicted in Fig. 1.1. This thesis focuses on the physical processes that act during this particular time, $\sim 10^5$ years after the gravitational collapse of a pre-stellar core. It is well accepted that planets form inside disks and that disks are important in the formation and evolution of stars. Planet formation is generally considered within disks in Stage II, but could start as early as Stage 0 and I if the conditions are favorable. Disk formation and its early evolution are not at all yet understood (e.g., Bodenheimer 1995; Williams & Cieza 2011; Li et al. 2014). The main questions of this thesis are as follows:

- Do disks like those observed around pre-main sequence stars exist in the embedded phase of star formation?
- Are they observable and how can they be differentiated from the infalling rotating envelope?
- Are their physical and chemical structure consistent with the current models of disk formation?
- How stable are embedded disks and can they sustain a high infall rate from their envelope?
- How much does the embedded disk contribute to the observed molecular lines?

1.1.1 Radiation: dust and gas

Inferring the properties of young stellar objects (YSOs) is typically done through the dust continuum radiation in images and spectral energy distribution (SED, see Fig. 1.1). The peak of the SED determines the dominant dust temperature of the system. Dust warms up by reprocessing the stellar radiation from high-energy (short wavelengths) to lower-energy photons (long wavelengths). The dust temperature structure is determined by the protostellar luminosity ($L_\star$) and the dust properties, through absorption and re-emission of photons. The widely adopted dust opacities for YSOs are given by Ossenkopf & Henning (1994). Furthermore, the bulk dominant dust sizes and mineralogy of dust grains are found to be similar in disks across different star-forming regions (e.g., Oliveira et al. 2010, 2011). The warm dust in the inner disk emits in the infrared. However, during the embedded phase of star formation, the cold massive envelope surrounds the disk and re-radiates the disk emission. For a given physical structure, a complete SED and image(s) at different wavelengths can be simulated using radiative transfer tools to interpret observations in continuum (Dullemond et al. 2007) and in lines (van der Tak 2011).

While the dust thermal emission indicates the bulk energetics that are present in the system, atomic and molecular lines are used to probe the bulk mass of the protostellar system. The universe is filled with a wide variety of molecules residing in clouds with different physical conditions (see Tielens 2013 for a review on the 'molecular universe'). The observable molecular emission can be split into three types of different transitions: electronic transitions, vibrational transitions, and rotational transitions. In this thesis, vibrational and rotational transitions of CO are discussed (see Fig. 1.2). Vibrational transitions are due to the release of energy from one rotational level within a vibrational state to a rotational level within a lower vibrational state by photon emission. The rotational transition is caused by the change of angular momentum of the molecule, which for a diatomic molecule is given by $E_{\rm J} = \frac{\hbar^2}{2\mu R_0^2} J\,(J+1)$ where μ is the reduced mass, R_0 is the equilibrium distance, and J is the quantum rotational number. The rotational levels can be populated through collisions with another molecule, which is H_2 in most cases while it is also possible to have H and electrons as collision partners. Thus, this gives a concept of critical density ($n_{\rm crit} = \frac{A_{\rm ij}}{\sum C_{\rm ij}}$, where $A_{\rm ij}$ is the Einstein coefficient and $C_{\rm ij}$ is the collisional rate coefficient), which describes a density regime where the density of the collisional partner is sufficient for the excitation to balance the spontaneous de-excitation. For densities larger than the critical density, the level populations are expected to be thermalized such that they follow the Boltzmann distribution with a given gas kinetic temperature (local thermal equilibrium or LTE). Most importantly, these transitions are quantized such that they are emitted at a certain frequency (i.e., CO $J = 1 - 0$ is at 115.271 GHz) and any gas motions are imprinted by introducing Doppler shifts. Hence, by observing frequency resolved lines, one can study the gas kinematics (e.g., Sargent & Beckwith 1987; Yen et al. 2013).

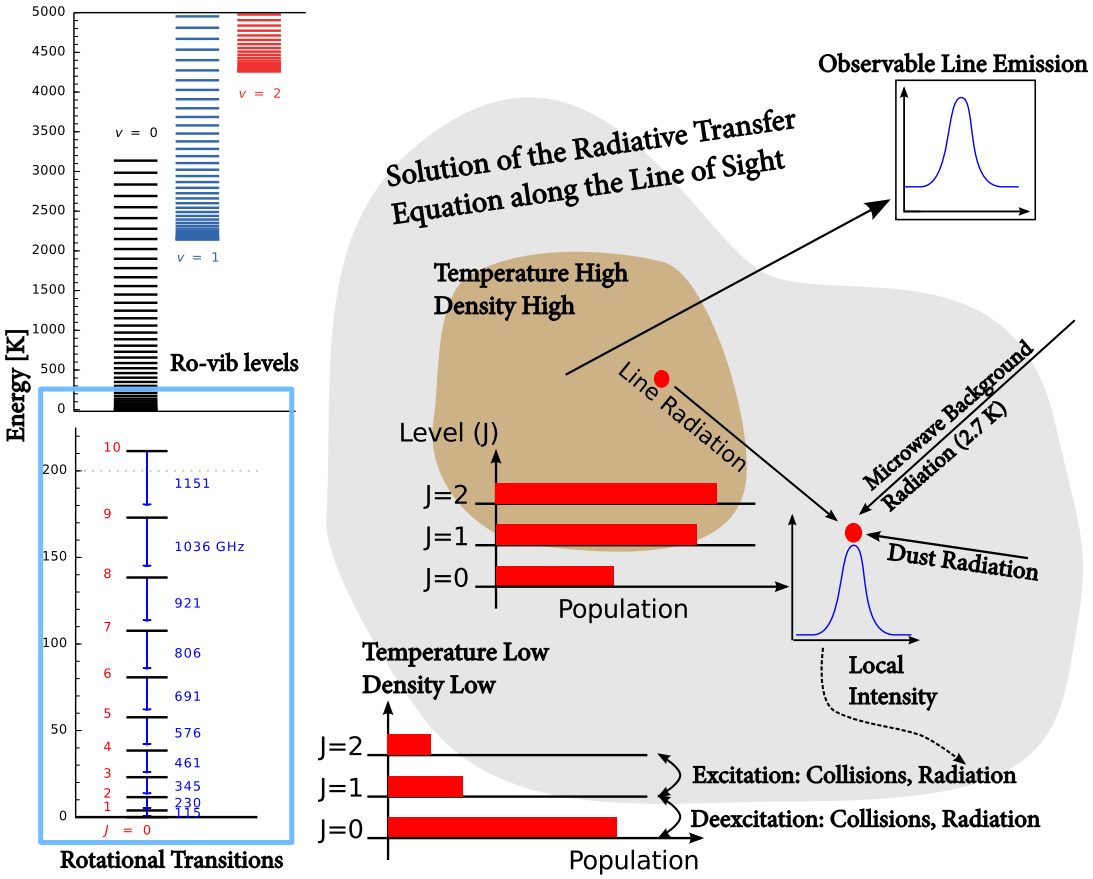

Figure 1.2 — *Top left:* The vibrational and rotational levels of ^{12}CO up to $v = 2$ and $J = 40$. *Bottom left:* A zoom in of the rotational transitions up to $J_u = 10$. A cartoon depicting the molecular line excitation and radiation propagation from an envelope to the observed line profile. The low J levels are populated in the low density and low temperature regimes while higher rotational levels are populated in dense warm gas. The excitation of molecular levels include collisions with H_2 (sometimes with H, He, and electrons) and radiation from dust, other CO molecules if sufficiently optically thick, and the cosmic microwave background at 2.7 K. Adapted from Bruderer 2010.

1.1.2 Observational tools

Disks in Stage II of star formation are directly observable through the SED. However, in the early stages of star formation, the SED is a combination of the dust thermal emission of both envelope and disk. In order to study the embedded disk, interferometric observations at longer millimeter wavelengths are needed to observe the thermal dust emission from the inner envelope where the disk resides. Interferometry is a technique in which signals from multiple telescopes are correlated in order to gain enough spatial resolution (see Fig. 1.3). Millimeter and submillimeter interferometric observations of dust and gas have been crucial in revealing the inner workings of star-forming regions. These telescopes are separated by certain baselines to cover different angular resolutions (0.5″–20″). A pair of telescopes with a short baseline is sensitive to large-scale structure while a pair that has a very long baseline can resolve the small-scale structures. By combining different configurations, one can simultaneously resolve all scales. These different scales correspond to (u, v)-distances in Fourier space that relate the spacing of a pair of telescopes to the source position. An image is obtained by the Fourier transform of a collection of (u, v) points. By utilizing the Earth's rotation, a more complete

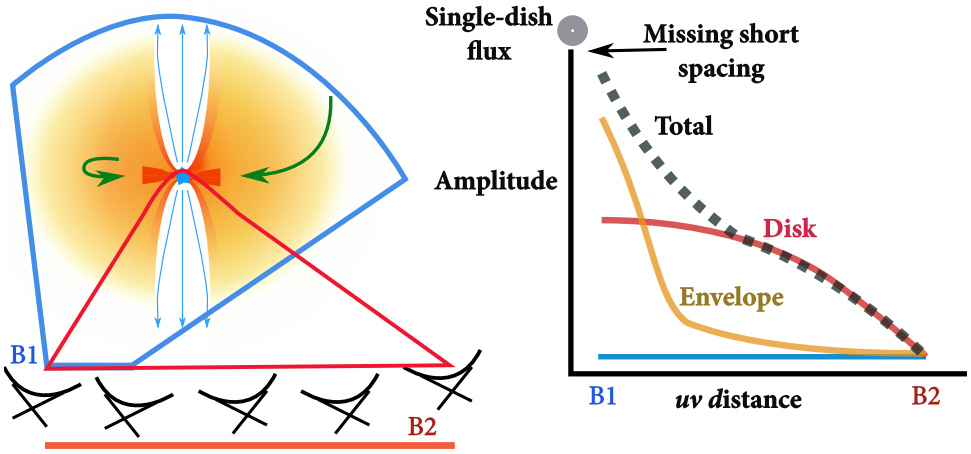

Figure 1.3 — *Left:* Sketch of how interferometry probes the physical structure of an embedded disk. A short baseline (*blue*) and a long baseline (*red*) are indicated. *Right:* The correlated flux as function of baseline length in terms of u, v distance is shown by the black dashed line. The expected contribution of the envelope and the disk are shown in orange and red, respectively. The single dish flux is indicated by the circle on top which could be larger than the correlated flux at short baselines.

(u, v) coverage can be obtained which greatly increases the image quality. On the other hand, the largest physical scale that one probes is defined by the shortest baseline. Consequently, emission from the large scale is always filtered out due to the missing short spacings since the telescopes cannot be placed infinitely close together. Beckwith et al. (1984) demonstrated the power of such observations when they revealed the compact structure of gas and dust around HL Tau. With the availability of the Plateau de Bure Interferometer (PdBI, 7 telescopes) and Atacama Large Millimeter Array (ALMA, 66 telescopes), such observations can be routinely done with much better sensitivity than before to reveal faint structures. Furthermore, the jump from 6 to 66 telescopes will provide unprecedented imaging capabilities at submillimeter wavelengths. The full ALMA will provide an angular resolution $< 0.1''$ or < 14 AU spatial resolution at typical distances of 140 pc, which is sufficient to study the disk formation process.

1.2 Disk formation: energy and momentum conservation

Significant theoretical work has gone into studying the disk formation process. Current observations provide the spatial resolution and sensitivity to test these theoretical models. The star formation process is very complex with dynamical processes occurring at physical scales ranging from a few stellar radii of $\sim$0.1 AU to envelope scales of 10^4 AU and densities of 10^4 cm^{-3} to 10^{15} cm^{-3}. The disk forms out of conservation of energy and momentum as the core collapses from the large-scale molecular cloud. This section introduces the basic idea of how this proceeds and the problems with current theories.

1.2.1 Large scale: envelope

The physical processes that control the collapse of a large scale protostellar core include turbulence, gravity, thermal pressure, rotation, and magnetic field. Turbulence is an important aspect of galactic dynamics as a whole. It is defined by chaotic, non-linear changes to density, velocity, temperature and magnetic field during energy transfer from large scale to smaller scales. Recent major advances in theoretical models of star formation have focused on the role of turbulence in star and disk formation simulations (Mac Low & Klessen 2004; McKee & Ostriker

2007). Gravity takes over once there is substantial mass within a sufficiently small volume. In the presence of gravity alone, the gas and dust simply stream toward the center. The presence of rotation changes the trajectory of the gas and dust as they spiral toward the growing protostar. In general, the dynamics at large scale are unchanged by rotation, however the densities and velocities are changed at small scales. Finally, magnetic fields permeate the galaxy and regulate the star-formation process (see e.g., McKee et al. 1993; Crutcher 2012). Its origin and how it is regulated is still debated. In reality, all of these forces act together during the dynamical evolution of the forming star and disk system. Fast and reliable computer programs are required to investigate the combined effects of all these forces.

Envelope rotation has been observed by Goodman et al. (1993) by mapping N_2H^+ emission on scales of $\sim$0.1 pc. The typical rotational rates of 10^{-13}–10^{-15} Hz seem to be consistent with that expected from turbulent cloud simulations by Burkert & Bodenheimer (2000). However, recent three-dimensional simulations by Dib et al. (2010) suggest that the inferred rotation rates from observations could be up to one order of magnitude higher than the true specific angular momentum of the core.

The strength of the magnetic fields toward molecular cloud cores has been inferred through statistical analysis of observations of the Zeeman effect (see e.g., Crutcher 2012). Sufficient magnetic pressure can prevent gravitational collapse when its mass is subcritical such that $M < M_{\phi_B} = \frac{\pi R^2 B}{2\pi\sqrt{G}}$ for a slab of gas and a uniform magnetic field B (Nakano & Nakamura 1978; McKee et al. 1993). In the supercritical case ($M > M_{\phi_B}$), the core simply collapses to form a star. The interesting case for a subcritical cloud is that the magnetic field prevents the ionized gas and dust from collapsing, but the neutral material can proceed to form a star (ambipolar diffusion, Zweibel 1988). More important for the disk formation and the trajectory of material is the fact that the presence of a magnetic field can remove angular momentum due to the twisted magnetic field lines. This strongly affects the formation of disks at scales $R < 1000$ AU as rotation dominates the motion on smaller scales than the magnetic fields.

1.2.2 Small scale: star and disk

The flow of material from the large-scale structure (> 1000 AU) to small scales (< 1000 AU) is determined by the angular momentum conservation and evolution. The sun's specific angular momentum is $\sim 10^{15}$ cm^2 s^{-1} (Pinto et al. 2011). For comparison, the typical specific angular momentum of molecular cloud cores is $\sim 10^{21-22}$ cm^2 s^{-1} (Goodman et al. 1993), so > 6 orders of magnitude need to be removed. This problem was first recognized by Mestel & Spitzer (1956). Perhaps, some of the angular momentum has already been lost either before or during the gravitational collapse such as described above through magnetic fields. Since angular momentum is strictly conserved in equations of motion, it needs to be transferred to other bodies or removed by other mechanism(s).

The infalling matter with excess angular momentum will form a flattened structure or a rotationally supported disk. Disks are found to have a typical specific angular momentum of $\sim 10^{19-21}$ cm^2 s^{-1}, which are lower than their envelope but still higher than the growing star (Williams & Cieza 2011; Belloche 2013). Consequently, the disk must further remove the angular momentum excess. It does so either by launching a wind/jet or by viscous transport. For the purpose of this thesis, viscous transport will be discussed. Viscosity can arise either from the collisions between gas molecules or the mixing of fluid elements through turbulence. The latter is the most commonly used viscosity parameter to describe the viscous evolution of disks while molecular collisions are unimportant. The most commonly used viscous disk evolution model is that of the alpha-disk (α prescription) as described by Shakura & Sunyaev

(1973). It is assumed that the energy loss and momentum transfer occurs locally within a length scale that corresponds to the disk's scale height ($H_{\rm disk}$). From such models, a constant $\alpha \sim 10^{-2}$ is found to be a good description of the observed disk evolution and physical structure (Hartmann et al. 1998; Hughes et al. 2011).

1.2.3 Infall and accretion

The embedded phase of star formation is the period in which both of the physics at large scale and at small scales are intertwined and affect each other. The trajectory of the infalling matter from the large scale dictates the distribution of matter that forms the disk. The physical structure of the disk is crucial in determining its accretion properties. Infall describes the general trajectory of gas and dust from the envelope to the disk or star. Accretion is the transport of material inward through the disk onto the star. In the embedded phase of low-mass star formation, the dominant heating comes from the combination of infall and accretion since the protostar is still growing. Hence, the dust temperature structure that affects the physical and chemical structure of the disk and the inner envelope (< 1000 AU) relies on the understanding of the rate at which the material is being transported onto the star. This process does not have to be continuous, but it is likely episodic to avoid the luminosity problem (e.g., Evans et al. 2009b; Dunham et al. 2014). The 'luminosity problem' describes the discrepancy between the observed luminosities of embedded protostellar systems and the luminosity produced by the accretion process at a steady rate needed to build up a solar mass star (see Kenyon & Hartmann 1990).

1.3 Simplified models of star formation

As described in previous sections, star formation involves a wide range of physical processes at both large scale (~ 0.1 pc) and small scale (< 100 AU). However, simplified models of star formation that only look at one or two physical processes, in general, capture the physical structure of the large-scale envelope and the disk. These physical structures are used to interpret the observational data. There are two types of simplified models of star formation: analytical models and hydrodynamic simulations.

1.3.1 Analytical models

A subset of these simplified models can be solved analytically to describe the general sequence of star formation (Shu 1977). A significant fraction of our understanding of star formation is obtained through investigation of how different, separated physical processes independently affect the collapse and disk formation. A few of the simplifications are presented here with an increasing level of complexity. The following sections introduce analytical models of disk and envelope around protostars.

1.3.1.1 Large-scale envelope

The simplest model of the large-scale envelope is a spherically symmetric power law model: $\rho \propto r^{-p}$ where ρ is the total (gas+dust) density, r is the spherical radius, and p is the power-law slope. Such a power-law model stems from earlier studies such as the collapse of a singular isothermal sphere (Larson 1969). The exact density profile may change depending on the polytropic equation of the gas ($P \propto \rho^{\gamma}$, see Ogino et al. 1999 for detailed discussion). Furthermore, the presence of magnetic fields slows down the contraction process that will eventually lead to the isothermal solution as shown by Shu (1977). The temperature structure of such a model can be determined by assuming a central protostar with a temperature of ~ 5000 K. Such a

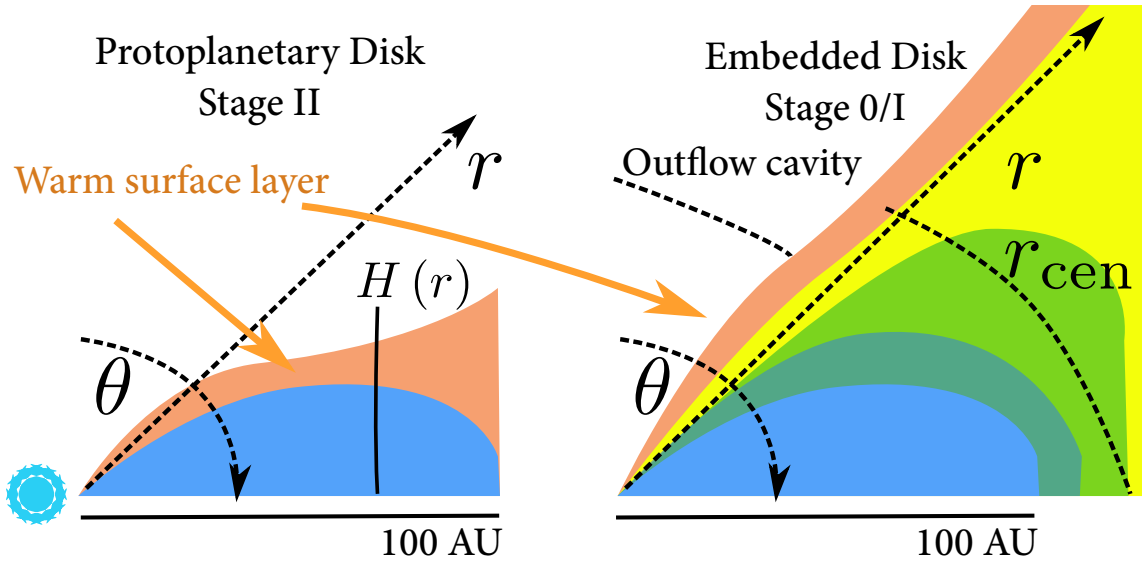

Figure 1.4 — Schematic of the 2D protoplanetary disk (*left*) and an embedded disk (*right*) physical structure in spherical coordinates (r, θ). The scale height of the disk $H(r)$ is indicated along with the warm surface layer that emits most of the IR irradiation. The outflow cavity and centrifugal radius $r_{\rm cen}$ are indicated in the embedded disk model.

model has been shown to reproduce the observed properties (SED and continuum images) of protostellar envelopes (e.g., Kenyon et al. 1993; Jørgensen et al. 2002).

The effects of rotation on the collapse process of the envelope were investigated in the early 70s using two- and three-dimensions with imposed axisymmetry (Larson 1972; Woodward 1978). Ulrich (1976) calculated the density structure of the envelope by imposing angular momentum conservation as the parcels of gas and dust fall toward the center. From these assumptions, the 2D density structure is described by the following equation:

$$\rho\left(r,\mu\right) = \rho_0 \left(\frac{r}{r_{\rm cen}}\right)^{-3/2} \left(1+\frac{\mu}{\mu_0}\right)^{-1/2} \left(\frac{\mu}{\mu_0}+\frac{2r_{\rm cen}}{r}\mu_0^2\right)^{-1}, \tag{1.1}$$

where $\mu \equiv \cos\theta$, $r_{\rm cen}$ is the centrifugal radius where the infalling material is stopped by centrifugal force, and finally μ_0, θ_0 is the solution to the streamline at r and θ from θ_0 (see Fig. 1.4, Cassen & Moosman 1981, Whitney & Hartmann 1993). The scaling factor ρ_0 could be a free parameter or connected to the infall rate from the envelope. Compared with the spherically symmetric power-law models, this particular model in 2D is similar at large scale (> 1000 AU) while the inner regions are flattened (disk-like). The flattened region is determined by the $r_{\rm cen}$ parameter which describes the regime in which the material starts to enter the disk, and, consequently, can be larger than the extent of the rotationally supported disk where the azimuthal velocities are Keplerian. Such a simple two-dimensional model has been used to model the observed properties of both dust and gas toward YSOs (e.g., Whitney & Hartmann 1993; Eisner 2012; Yen et al. 2013).

1.3.1.2 Flaring disk

At small scales (< 100 AU), an accretion disk forms. The density and velocity structures described above tend to break down when comparing to observations that probe the inner regions. In 1D, the disk's axisymmetric physical structure is generally described by (e.g., Beck-

with et al. 1990; Fedele et al. 2013):

$$\Sigma = \Sigma_0 \left(\frac{r}{r_0}\right)^{-p}, \; T = T_0 \left(\frac{r}{r_0}\right)^{-q}, \tag{1.2}$$

where Σ is the dust surface density, and T_0, Σ_0, and r_0 are the scaling factors where T can refer to either the dust or gas temperature. Such parametric models are found to reproduce most of the observed gas and dust emission from disks at both short and long wavelengths. Disk flaring is required to account for some missing flux emitted from the surface layer at mid-infrared wavelengths which is warmer than the disk's midplane (see Fig. 1.4, Kenyon & Hartmann 1987; Dullemond et al. 2007). A full detailed vertical structure calculation of disks is typically needed to reproduce both continuum and molecular line data (see Chiang et al. 2001; Dullemond et al. 2007). The general 2D accretion disk model is described by

$$\rho\left(r,\theta\right) = \frac{\Sigma}{\sqrt{2\pi}H} \exp\left(-\frac{r^2 \cos\theta^2}{2H^2}\right), \tag{1.3}$$

where $H = H_0 \left(\frac{r}{r_0}\right)^h$ is the scale height of the disk with a power-law exponent $h \sim 9/7$ (see Fig. 1.4, Chiang & Goldreich 1997). With the increased of computing power, 2D disk models are routinely used to model the observed dust and gas emission from disks including vertical hydrostatic equilibrium or a parametrized flaring index (Williams & Cieza 2011 and references therein).

1.3.1.3 Disk formation and evolution: time-dependence

Terebey et al. (1984) calculated the collapse of a rotating singular isothermal sphere. Cassen & Moosman (1981) focused on the early build up and evolution of disks using the streamline of particles from the large-scale envelope in the embedded phase of star formation. The merging of these two solutions describes the time-dependent analytical solution of disk formation in the absence of magnetic fields and turbulence. Such models have been coupled to protostellar evolution models to include the heating from a growing protostar. These types of models have been used to predict the observed evolutionary properties of YSOs (e.g., Young & Evans 2005). Visser et al. (2009) coupled such time-dependent models with simple chemistry to look at the chemical changes that take place as the disk forms and their connection to the chemical inventory of comets.

A semi-analytical description of the collapse including magnetic fields was given by Galli & Shu (1993). They showed that a 'pseudodisk' forms when the collapse proceeds in the presence of magnetic fields. A 'pseudodisk' is an infalling flattened density structure that can extend up to ~ 1000 AU due to preferential mass settling along field lines toward the equatorial plane. This differs from a 'true' disk whose angular velocity is Keplerian and radial velocity is defined by the viscous transport. Efficient magnetic breaking poses a problem for disk formation in the case of ideal magnetic forces as the disk is not rotationally supported (Galli et al. 2006; Li et al. 2014). Similar results are obtained from 3D magneto-hydrodynamic (MHD) simulations.

The path that the material takes as it spirals down to the central protostar strongly affects the chemical structure of the disk. It is also found that complex molecules tend to be enhanced if a rotationally supported disk is present instead of a pseudodisk. This occurs due to the lack of photodissociating photons coupled with a sufficiently warm disk for complex molecules to form. Therefore, continuum and molecular line observables that can differentiate between the two modes of disk formation are required to connect the physical and chemical changes during the early stages of star formation to our Solar System.

1.3.2 Numerical hydrodynamic simulations

Recent progress in numerical simulations of star formation has been made due to advances in computing. While analytical solutions can describe the general features of star formation, hydrodynamic simulations can investigate the non-linear effects of the different physical processes at once. However, one should be cautious of the numerical artefacts that are inherent in these simulations. In general, there are three types of numerical simulations that one can adopt: smoothed particle hydrodynamics (SPH), grid-based, and moving mesh. The two most tested and benchmarked of these are SPH and grid-based. There are indeed fundamental differences in the two methods as described in Agertz et al. (2007) and Tasker et al. (2008). In this thesis, SPH and grid-based codes are used.

1.3.2.1 Smoothed Particle Hydrodynamics (SPH)

This method solves the equations of fluid dynamics by interpolation (smoothed) between many dynamic particles. The implementation was started roughly 40 years ago by Lucy (1977) and Gingold & Monaghan (1977). In recent years, the treatment of different physical processes including magnetic fields has been added which are reviewed in Springel (2010) (see also Monaghan 1992 for an introduction to SPH). Any physical properties such as density (ρ), temperature described by sound speed $c_{\rm s}$, and velocities are calculated through kernel W smoothing such that

$$\rho\left(\bar{r}\right) = \int \rho\left(\bar{r}\right) W\left(\bar{\delta r}, h_{\rm SPH}\right) d\bar{r'} = \sum_{\rm i} \rho_{\rm i} W\left(\bar{\delta r}_{\rm i}, h_{\rm SPH}\right) \tag{1.4}$$

with $\bar{r}$ the position of the particle i and $h_{\rm SPH}$ the smoothing length. Most current codes adopt a cubic smoothing kernel based on the distance normalized by the smoothing $h_{\rm SPH}$. This method follows the particles as they move through space and time (Lagrangian method), which ensures the conservation of energy and momentum. SPH has been used to simulate star formation, stellar encounters, planet formation, and disk evolution.

1.3.2.2 Grid methods and AMR

Grid-based codes fix the number of resolution elements in which the fluid equations are solved. Thus, the equations of motions are solved within a set of boundary conditions and information (transfer of mass, energy, and momentum) must be propagated to adjacent grids (Eulerian) through numerical schemes. Adaptive-mesh refinement (AMR) splits up or refines certain grid(s) that satisfy a few pre-defined conditions in order to resolve the physics within that region. Different methods have been used to propagate information from one cell to nearby cells such as those (and variations of them) in van Leer (1979), Woodward & Colella (1984), and Stone & Norman (1992). In particular, Fleming et al. (2000) introduced methods to solve non-ideal magneto-hydrodynamics (MHD) equations. In the ideal MHD limit, the magnetic field is always frozen to the fluid element, while in the non-ideal case, the field is allowed numerically to diffuse and reconnect. Non-ideal MHD treatment is found to allow for rotationally supported disk formation, although not conclusively.

1.3.3 Parallelization

Recent advances in computing allow for large dynamic range (few pc down to few AU) star formation simulations to be performed. Most of these calculations can be done more efficiently by performing them in parallel using multiple central processing units (CPUs). There are two types of parallelization that have been used in this thesis: multicore computing and cluster

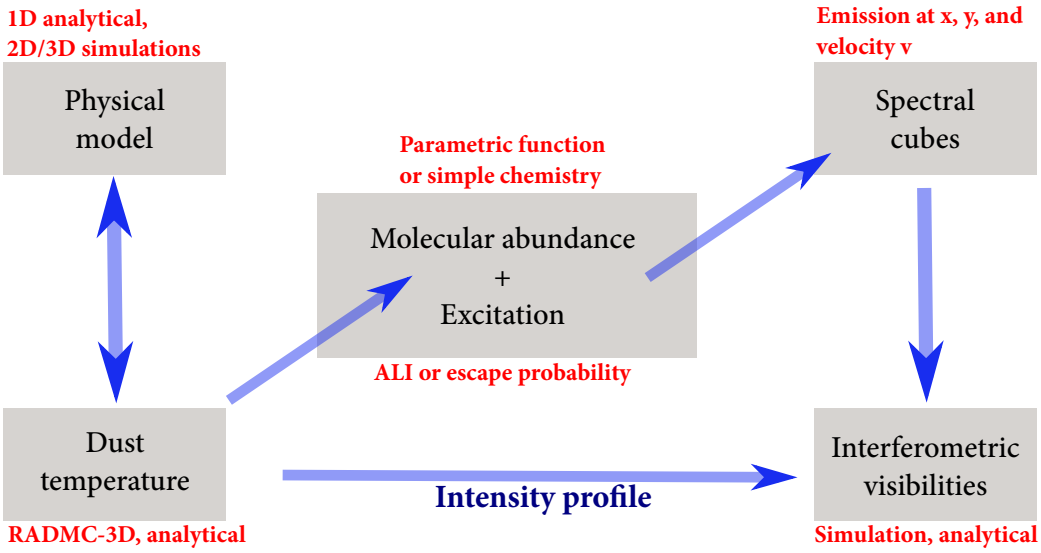

Figure 1.5 — Flowchart indicating the steps taken to generate observables in both continuum and molecular gas lines. The methods are indicated in red. The analytical physical models are listed in § 1.3. Simulations of interferometric visibilities are performed with *Common Astronomy Software Applications* (CASA) and GILDAS. Analytical calculations of visibilities are described in Chapter 5.

computing. Multicore computing describes a method in which a computational task is distributed over multiple cores in one desktop computer. Cluster computing is made out of several desktops that are connected within a local area network. Even when the hardware is available, a parallel programming language is required to instruct tasks and memory distribution.

Most of the parallelization done during this thesis was performed using the built-in *multiprocessing* in Python. This is done by distributing a number of tasks such as the simulation of $\geq$30 rotational or ro-vibrational molecular transitions over many CPUs. The hydrodynamical codes mostly have the Message Passing Interface (MPI) language built in them. For example, using MPI, the particles in SPH simulations are distributed over different CPUs. Each of the CPUs then calculates the forces acting on the particles, then the updated properties are communicated to other CPUs to inform other tasks for the next iteration. Finally, another parallelization software is Open Multi-Processing (OpenMP). OpenMP is typically used within a repeated task (e.g., photon propagation or solving radiative transfer equations at one pixel/velocity). The software then distributes a task or a loop over the specified number of threads and CPUs. Most of the molecular line radiative transfer calculations were parallelized using multicore computing while the hydrodynamic simulations were performed on a cluster of computers.

1.4 Bridging theory and observations

A suite of radiative transfer tools is required to bridge the theoretical models described in previous sections to observations. One radiative transfer tool is needed to calculate the dust temperature structure by simulating the photon propagation through dusty media. Another set of radiative transfer tools is required to simulate the molecular line emission. In most cases, these two tools are completely independent of each other. The typical flow of modelling the observables is illustrated in Fig. 1.5.

1.4.1 Radiative transfer: dust and masses

Dust makes up about 1% of the total mass. For a given central heating and mass distribution as in § 1.3, dust continuum radiative transfer simulates the propagation of photons as they are absorbed or scattered and re-emited by dust. The most common method is the Monte Carlo (MC) approach (Bjorkman & Wood 2001) where photon packages with energy $L_\star/N_{\rm photons}$ are launched from the central source. Through the absorption and re-emission of these photon packages, the dust temperature structure can be obtained. The amount of energy that the dust absorbs depends on the dust optical properties.

The photon propagation is easy computationally for optically thin radiation. In this thesis, a few tricks are used to efficiently compute the dust temperature structure of optically thick ($\tau \geq 10^6$) embedded disks. Computationally, regions are taken as optically thick, when the opacity towards the star is larger than a few 1000 at the peak wavelength of the star. In general, a higher number of photons ($\sim 10^7$) are required to obtain a smooth dust temperature structure. The exact number of photons depends on the number of grids. The propagation of a photon through an optically thick region is modified such that it is not trapped within one computational cell (see Min et al. 2009). An additional source of heating such as accretion heating can be added. There are two ways to add such a term, either by depositing the energy that each cell has or by launching another set of photons from the disk. Furthermore, the diffusion approximation ($\nabla \frac{\nabla T^4}{3\rho\kappa_{\rm P}} = 0$, where $\kappa_{\rm P}$ is the Planck opacity) is used to smooth the midplane's temperature structure. The diffusion approximation is valid in the highly optically thick region ($\tau_{0.1\ \mu{\rm m}} >> 1$) since the radiation field is in thermal equilibrium such that the source function is the Planck function. A smooth dust temperature structure is crucial in the determination of molecular abundances in embedded disks.

The dust thermal emission can be simulated by solving the radiative transfer equation along a line of sight similar to that depicted in Fig. 1.2. One generally finds that the emission at long wavelengths is optically thin and, consequently, it is a direct measure of the dust mass. Disk and envelope masses have been obtained through such assumptions. The simplest envelope model is by assuming spherical symmetry ($\rho \propto r^{-p}$). Through dust continuum radiative transfer programs such as *DUSTY* (Ivezic & Elitzur 1997), the thermal structure can be obtained and its SED compared to observation. Jørgensen et al. (2002) and Kristensen et al. (2012) used such a method to constrain the large-scale envelope structure. In order to determine the disk mass, Jørgensen et al. (2009) explored the contribution of such a model to interferometric dust thermal emission. Thus, by accounting for the large-scale contribution, the disk emission can be extracted and, in turn, their masses (see also Looney et al. 2003; Enoch et al. 2011). More sophisticated tools such as RADMC (Dullemond & Dominik 2004), RADMC-3D, and Hyperion (Robitaille 2011) are required to build 2D and 3D physical models. Recent developments in 3D radiative transfer tools are reviewed by Steinacker et al. (2013).

1.4.2 Chemical abundances

To simulate the observed molecular lines, the gas phase molecular abundances are needed. A simple gas phase abundance can be obtained by considering the adsorption and thermal desorption of molecules on the dust grains. In addition, a lower abundance is expected along the warm surface layers close to the star (see Fig. 1.4) where molecules can be photodissociated by absorption of energetic ultraviolet (UV) photons (see van Dishoeck et al. 2006). Ices could also be photodesorbed from the grain if they are not well shielded from energetic UV photons (e.g., Öberg et al. 2009; Fayolle et al. 2011). This thesis limits the chemistry to adsorption and thermal desorption of molecules on the dust grains. The adsorption rate is the rate at which

ices of species X accumulate on the dust grain given the gas temperature and size of the dust (~ 0.1 μm). A molecular species X also has a binding energy that describes how strongly it is bound on the grain surface. The binding energies of well known ice species such as H_2O and CO have been inferred through controlled laboratory experiments (e.g., Bisschop et al. 2006; Burke & Brown 2010). At steady state, the adsorption rate $k_{\rm ads}$ is balanced by the thermal desorption rate $k_{\rm thdes}$. Using such a balance, one finds that CO is in the gas phase for $T_{\rm dust} > 20$ K while it is 100 K for H_2O. The temperature of this transition is pressure dependent such that it can be up to 160 K for H_2O at high densities ($n_{\rm H} \sim 10^{16}$ cm^{-3}). This is not necessarily valid at low densities such as those found in the large-scale envelope since the adsorption timescale is longer than the lifetime of the residing material. The physical processes such as infall tend to occur on timescales much shorter than the chemical timescales for the embedded phase of star formation. However, for most of the purposes of this thesis, steady state chemistry is appropriate to simulate the observables from theoretical models.

1.4.3 Molecular emission as a probe of physical structure

The dust physical structure is the first step in the determination of molecular abundances toward YSOs (e.g., Hogerheijde et al. 1998; Yıldız et al. 2013). While the low-J transitions of CO can be treated in local thermal equilibrium (LTE or thermalized) due to their low critical densities, higher-J lines tend not to be in LTE. Non-LTE population levels are calculated by considering different excitation and de-excitation mechanisms (van der Tak et al. 2007):

$$n_{\rm i} \sum_{\rm i}^{\rm N} P_{\rm ij} = \sum_{\rm j\neq i}^{N} n_{\rm j} P_{\rm ji}, \tag{1.5}$$

where $n_{\rm i,j}$ are the populations of levels i and j, respectively, N is the total number of levels, and $P_{\rm ij}$ indicate the rate of transition between level i and j. The rates take into account the probability of spontaneous emission given by Einstein $A_{\rm ij}$ coefficient, probability of stimulated emission $B_{\rm ij}\left\langle J_{\rm ij}\right\rangle$, and collisional rates.

Thanks to many years of primarily theoretical studies in determination of potential energy surfaces and the subsequent collision dynamics on these surfaces, these properties are known and tabulated in the *Leiden Atomic and Molecular Database* (LAMDA Schöier et al. 2005) for well-known molecules. Theoretical calculations of collisional rate coefficients typically employ the close coupling (CC), coupled-states (CS) and infinite order sudden (IOS) approximations. While CC is exact, the CS approximation assumes that the angular momentum is conserved and the IOS approximation assumes that the molecules do not rotate during collision (see Schöier et al. 2005; Roueff & Lique 2013). Most recent calculations employ the CC method, which solves the nuclear Schrödinger equation exactly given the detailed potential energy surfaces (Roueff & Lique 2013). Most of the molecular databases only contain collisional rate coefficients for the rotational levels within the vibrational ground state. For example, Yang et al. (2010) calculated the CO collisional rate coefficients up to $J = 40$. To reproduce recent observations of high-J CO molecular lines ($J > 40$), extrapolations are needed as used in Chapter 4 to calculate the population levels of $J > 40$ (see also Neufeld 2012). For a simple rigid rotor such as CO, the extrapolation considers the cross section of a linear molecule with an atom as described by a scattering matrix in the IOS approximation $S_{\rm l}(\theta|E) = \sum_{\rm L} S_{\rm L}^{\rm l} P_{\rm L}(\cos\theta)$ where $P_{\rm L}$ is the Legendre polynomial of L degree at energy E. The generalized CS cross section for a linear rigid rotor

colliding with a spherical rigid body is given by

$$\sigma_n\left(j_{\rm a}' j_{\rm b}'|j_{\rm a} j_{\rm b}|E\right) = \frac{\pi}{k^2}\sum_{lmm'}(2l+1)\begin{pmatrix} j_{\rm a} & j_{\rm b} & n \\ m & -m' & m'-m\end{pmatrix}\begin{pmatrix} j_{\rm a}' & j_{\rm b}' & n \\ m & -m' & m'-m\end{pmatrix} \times(-1)^{j_{\rm b}+j_{\rm b}'}\sqrt{\frac{2j_{\rm a}'+1}{2j_{\rm a}+1}}\left|\delta_{j_{\rm a}j_{\rm a}',j_{\rm b}j_{\rm b}'}-S^{\rm l}_{jm}\right|^2, \quad (1.6)$$

where $j_{\rm a,b}$ are the rotational quantum numbers, m is the magnetic quantum number, l describes the orbital angular momentum, $()$ is Wigner's 3-j symbol, δ is the Kronecker delta symbol, and n describes the tensor rank for the relaxation mechanism at a given energy E (see Goldflam et al. 1977). $S^{\rm l}_{\rm jm}$ is the scattering matrix represented by the basis vectors $|jm>$ such that $S^{\rm l}_{\rm jm} = < j'm'|S|jm >$. The inelastic collisional relaxation is dominated by $n = 0$ since there is no change in rotation as consequence of the IOS approximation, which in turn simplifies most of these terms. This simplification leads to the following relation

$$C(T|J_{\rm u}\rightarrow J_{\rm l},\Delta v=0) = (2J_{\rm l}+1)\sum_{J=|J_{\rm u}-J_{\rm l}|}^{J_{\rm u}+J_{\rm l}}\begin{pmatrix} J_{\rm u} & J_{\rm l} & J \\ 0 & 0 & 0\end{pmatrix}^2 \times C(T|J_{\rm u}\rightarrow 0,\Delta v=0), \quad (1.7)$$

where $C(T|J_{\rm u}\rightarrow 0)$ is the collisional rate coefficient from $J_{\rm u}$ to the ground rotational state at kinetic temperature T without a change of the vibration level. Such extrapolations can be extended to include vibrational levels and to approximate the collisional rate coefficients for tri-atomic linear molecules (e.g., Chandra & Sharma 2001).

Once the abundances are known, the non-LTE population levels can be treated in two ways. The Monte Carlo Accelerated Lambda Iteration technique (ALI) employed by Hogerheijde & van der Tak (2000) and Brinch & Hogerheijde (2010) can be used to iteratively find the radiation field ($\langle J_{\rm ij}\rangle$). The rate of stimulated absorption and decay depends on it (see Fig. 1.2), thus the problem of finding the radiation field and the level population is coupled. A faster method is by adopting the escape probability approach that considers whether the photon has escaped or is absorbed at another location which depends on the optical depth of the transition (Bruderer et al. 2012, and references therein).

With recent observations obtained with *Herschel Space Observatory*, it is possible to observe CO transitions up to rotational levels of ≥ 40. A recent survey of molecular emission toward young embedded objects has been conducted as part of the Water in Star-forming Regions with Herschel (WISH van Dishoeck et al. 2011) and Dust, Ice, and Gas in Time (DIGIT, PI: Evans) key programs. Through the modelling of ^{13}CO and C^{18}O emission up to the $J = 9$–8 transition toward one particular region, Yıldız et al. (2013) constrained the CO abundance structure in the large-scale envelope. Visser et al. (2012) included the UV heating of the gas such that $T_{\rm gas} > T_{\rm dust}$ in order to explain the observed high-J ($J_{\rm u} > 16$) fluxes. The high-J emission arises from the thin warm layer along the outflow cavity wall (see Fig. 1.4). Thus, the excitation and the simulated emission are sensitive to the setup of the computational cells along the cavity wall. With the access to such highly excited rotational transitions, it is then possible to probe different excitation conditions and, thus, the range of gas temperature within the envelope.

1.5 This thesis and outlook

This thesis explores both the theoretical and observational aspects of disk formation during the embedded stage of star formation. Semi-analytical and numerical hydrodynamic models have been coupled to dust continuum and line radiative transfer tool(s) as depicted in Fig. 1.5. The predicted spectrally resolved rotational transitions of CO isotopologs are simulated for comparison with observations. These simulations and predictions are accompanied by spatially and spectrally resolved observations of optically thin CO emission toward less embedded (more evolved Stage I) young stellar objects. The observations were carried out with the Plateau de Bure Interferometer (PdBI) located in France. The following list outlines the results of this thesis.

- The continuum and molecular line observables obtained from 3D MHD disk formation simulations are compared with 2D axisymmetric models in **Chapter 2**. The two MHD simulations differ in their initial magnetic field orientation: the magnetic field vector is aligned with the rotation axis in one case while it is strongly misaligned in the other (90°). These two represent the extreme outcomes of 3D MHD simulation of disk formation in which the simulation with the aligned magnetic field vector inhibits the formation of a Keplerian disk (see § 1.3.1.3). The 2D semi-analytical models are the same as described in § 1.3.1.3. The comparison shows that spatially resolved continuum observations at ~ 15 AU scale are required to determine the presence of Keplerian disks solely by continuum. This problem is alleviated if it is accompanied with spatially and spectrally resolved molecular line emission. The kinematical signatures of a pseudodisk are different from that of a rotationally supported disk if observed with sufficient spatial resolution (15 AU). Furthermore, these kinematics tend to give a good estimate (within a factor of 2) of their respective stellar masses.
- During the earliest stages of the embedded phase, the disk can be cold and massive, and thus prone to gravitationally instability. In addition, such gravitationally unstable disks are embedded inside an infalling envelope. To study the effect of infalling material onto the disk, the SPH (§ 1.3.2.1) code GADGET2 (Springel 2005) has been used to simulate such a scenario in **Chapter 3**. The angular momentum transport within the disk is enhanced by the infalling material without any fragmentation under the adopted cooling prescription. The simulation suggests that under such a scenario, a relatively low mass disk ($M_{\rm d}/M_\star \sim 0.1$) can undergo a high accretion rate driven by gravitational instability.
- As shown in Chapter 2, spectrally and spatially resolved molecular lines are the key in detecting embedded Keplerian disks. The new observational data from *Herschel*, APEX, and ALMA allow for access to highly excited rotational transitions of CO lines for the first time that probe the inner warm and dense gas (see Fig. 1.2). Thus, it is timely to provide predictions from theoretical models. **Chapter 4** focuses on the predicted evolution of molecular line observables from 2D axi-symmetric disk formation models with three different initial conditions that change the final disk properties. Similar to the result of Chapter 2, the ^{13}CO and C^{18}O $J_{\rm u} \geq 6$ lines can be broadened by the infall process. The excitation temperatures of CO within typical single-dish beams ($\geq 9''$), however, do not change with time, in contrast with the dust temperature as observed and predicted through the spectral energy distribution. The molecular line simulations are extended to include the near-IR ro-vibrational fundamental (Δv = 1) CO absorption lines at ~ 4.5 μm as observed by VLT CRIRES. The ro-vibrational excitation is found to evolve with time following the dust temperatures.

- Chapters 2 and 4 suggest that the deeply embedded disk is easily revealed by spatially and spectrally resolved molecular line observations. Furthermore, the disk's contribution to the integrated optically thin CO line is predicted to be high during the later phase of the embedded stages of star formation. **Chapter 5** presents the spatially and spectrally resolved ^{13}CO and C^{18}O 2–1 lines toward four well-known Stage I embedded objects in the nearby Taurus molecular cloud (d=140 pc). At a spatial resolution of $\leq 0.8''$ (~ 110 AU diameter), three out of the four targeted sources have ~ 100 AU radius Keplerian disks as traced by the C^{18}O 2–1 line. The properties of the claimed embedded disks in the literature combined with the sources studied in this chapter are compared with the 2D disk formation models of Chapter 4. This comparison suggests that the models with initial rotation of $\Omega = 10^{-14}$ Hz and slow sound speeds match well with the observed disks.
- As a consequence of an actively accreting disk, the energy dissipated away during the angular momentum transfer heats up the disk's midplane (viscous heating). This affects the regions where ices can survive on the dust grains (snowlines). **Chapter 6** presents a theoretical study of the snowlines of the major volatile ice species (H_2O, CO, CO_2) within an actively accreting embedded disk (see Fig. 1.4). Water is particularly relevant because the location of the water snowline is important for grain growth and planet formation. Water vapor emission has been recently detected toward embedded YSOs arising from the inner 50 AU diameter. This chapter explores whether such an embedded accreting disk model (§ 1.3.1) can explain the observed emission. The water snowline is located at >20 AU radius for a highly accreting disk ($\dot{M} \geq 10^{-5}\ M_\odot$ yr^{-1}). CO_2 can be in the gas phase up to ~ 40 AU at low accretion rates while CO is generally expected to be in the gas phase throughout the disk. The observed strength of optically thin water emission can be reproduced by the models. However, the models can only attribute the water emission to the disk for emission extending up to 30 AU.

The main conclusions of this thesis drawn from all of the chapters are as follows:

- Subarcsec spatially resolved line observations can distinguish rotationally supported disks from pseudodisks found in MHD simulations (*Chapter 2*).
- Excitation temperatures as derived from single-dish rotational transitions of CO do not evolve with time contrary to the dust continuum emission (*Chapter 4*).
- Rotationally supported disks up to 100 AU are likely present in the majority of embedded young stellar objects by the end of the collapse process. Semi-analytical models of disk formation can reproduce the disk radii found in these and even younger systems for modest initial rotation rates and sound speeds (*Chapters 4* and *5*).
- Embedded disks can undergo a high accretion rate due to the interaction with the infalling rotating envelope. Such interaction creates a non-axisymmetric disk that affects the chemical structure and evolution during the early stages of disk formation and evolution (*Chapters 2* and *3*)
- The inner 30 AU of an actively accreting embedded disk is characterized by warm dust temperatures ($T_{\rm dust} > 100$ K). Such high temperatures allow for major volatile ice species to be in the gas phase, which can recondense when the disk cools. Consequently, the chemical content inherited from the collapsing envelope could be reset. The hot young solar nebula scenario can only occur during Stage 0 phase of star formation, not during the Stage II phase (*Chapter 6*).

Future outlook Current observations have revealed the presence of rotationally supported disks in the inner few 100 AU toward a couple of embedded protostars (Tobin et al. 2012; Murillo et al. 2013), which are compared with disk formation models. However, to further study the details of the disk formation and evolution process in the earliest stages of star formation, the spatial resolution and sensitivity of ALMA down to scales of 10 AU is required. The higher spatial and spectral resolution observations of molecular lines can differentiate the Keplerian disk from the infalling envelope. The temperature structure of the disk, which is crucial to investigate the heating processes, requires two different molecular transitions of a molecule to investigate their excitation conditions. Furthermore, high sensitivity observations are necessary to study the velocity structure of the disk since the molecular emission at high velocities is much weaker than at line center. This will be easier done in the future to reveal the kinematics at small scales and allow disk tomography in radial and vertical direction. In addition, the combination of short and long baselines that ALMA can deliver will reveal the kinematics of the gas as it falls onto the disk.

This thesis employs steady-state accretion models of disk formation to investigate the molecular excitation. It is known that the accretion process is episodic during the early stages of star formation (Vorobyov et al. 2013; Dunham et al. 2014). The processes within the disk and the movement of the gas and dust during this phase has direct consequences for the physical and chemical structure of an evolving embedded disk (Visser & Bergin 2012; Jørgensen et al. 2013). The main challenge is to couple these simulations that include the disk's vertical structure with radiative transfer tools and chemical models to compare with observations.

Time dependence is needed to investigate the true gas and ice abundances that are present within the Keplerian disk. Time dependent radiative transfer and chemical models such as that applied to the 2D models need to be coupled with MHD simulations of disk formation. Furthermore, the comparison between the disk formation scenarios with and without turbulence is still an unexplored territory. The different scenarios also predict different protostellar formation histories that dictate the heating events during the early stages of star formation and, thus, the temperature structure of the newly formed disk. The predicted observables from the hot gas in the inner envelope and disk can be compared with observations that will be taken by the *James Webb Space Telescope* (JWST). The synergy between ALMA, VLT CRIRES, JWST, and ultimately E-ELT METIS will reveal the physical and chemical structure of the young disk at all scales, including the planet forming zones.

Bibliography

Agertz, O., Moore, B., Stadel, J., et al. 2007, MNRAS, 380, 963

André, P., Di Francesco, J., Ward-Thompson, D., et al. 2014, in Protostars and Planets VI, ed. H. Beuther, C. Dullemond, & T. Henning (Univ. of Arizona Press, Tucson), in press

André, P., Men'shchikov, A., Bontemps, S., et al. 2010, A&A, 518, L102

Arce, H. G., Shepherd, D., Gueth, F., et al. 2007, in Protostars and Planets V, ed. B. Reipurth, D. Jewitt, & K. Keil (Univ. of Arizona Press, Tucson), 245–260

Bachiller, R. & Tafalla, M. 1999, in NATO ASIC Proc. 540: The Origin of Stars and Planetary Systems, ed. C. J. Lada & N. D. Kylafis, 227

Batalha, N. M., Rowe, J. F., Bryson, S. T., et al. 2013, ApJ, 204, 24

Beckwith, S., Skrutskie, M. F., Zuckerman, B., & Dyck, H. M. 1984, ApJ, 287, 793

Beckwith, S. V. W., Sargent, A. I., Chini, R. S., & Guesten, R. 1990, AJ, 99, 924

Belloche, A. 2013, in EAS Publications Series 62, 25–66

Bergin, E. A. & Tafalla, M. 2007, ARA&A, 45, 339

Bisschop, S. E., Fraser, H. J., Öberg, K. I., van Dishoeck, E. F., & Schlemmer, S. 2006, A&A, 449, 1297

Bjorkman, J. E. & Wood, K. 2001, ApJ, 554, 615

Bodenheimer, P. 1995, ARA&A, 33, 199

Brinch, C. & Hogerheijde, M. R. 2010, A&A, 523, 25

Bruderer, S. 2010, PhD thesis, ETH Zurich

Bruderer, S., van Dishoeck, E. F., Doty, S. D., & Herczeg, G. J. 2012, A&A, 541, A91

Burke, D. J. & Brown, W. A. 2010, Phys. Chem. Chem. Phys., 12, 5947

Burkert, A. & Bodenheimer, P. 2000, ApJ, 543, 822

Cassen, P. & Moosman, A. 1981, Icarus, 48, 353

Chandra, S. & Sharma, A. K. 2001, A&A, 376, 356

Chiang, E. I. & Goldreich, P. 1997, ApJ, 490, 368

Chiang, E. I., Joung, M. K., Creech-Eakman, M. J., et al. 2001, ApJ, 547, 1077

Crutcher, R. M. 2012, ARA&A, 50, 29

Dib, S., Hennebelle, P., Pineda, J. E., et al. 2010, ApJ, 723, 425

Dullemond, C. P. & Dominik, C. 2004, A&A, 421, 1075

Dullemond, C. P., Hollenbach, D., Kamp, I., & D'Alessio, P. 2007, in Protostars and Planets V, ed. B. Reipurth, D. Jewitt, & K. Keil (Univ. of Arizona Press, Tucson), 555–572

Dullemond, C. P. & Monnier, J. D. 2010, ARA&A, 48, 205

Dunham, M. M., Stutz, A. M., Allen, L. E., et al. 2014, in Protostars and Planets VI, ed. H. Beuther, C. Dullemond, & T. Henning (Univ. of Arizona Press, Tucson), in press

Eddington, A. S. 1937, The Observatory, 60, 99

Eisner, J. A. 2012, ApJ, 755, 23

Enoch, M. L., Corder, S., Duchêne, G., et al. 2011, ApJ, 195, 21

Evans, N., Calvet, N., Cieza, L., et al. 2009a, ArXiv e-prints

Evans, II, N. J., Dunham, M. M., Jørgensen, J. K., et al. 2009b, ApJ, 181, 321

Fayolle, E. C., Bertin, M., Romanzin, C., et al. 2011, ApJ, 739, L36

Fedele, D., Bruderer, S., van Dishoeck, E. F., et al. 2013, ApJ, 776, L3

Fleming, T. P., Stone, J. M., & Hawley, J. F. 2000, ApJ, 530, 464

Galli, D., Lizano, S., Shu, F. H., & Allen, A. 2006, ApJ, 647, 374

Galli, D. & Palla, F. 2013, ARA&A, 51, 163

Galli, D. & Shu, F. H. 1993, ApJ, 417, 220

Gibb, E. L., Whittet, D. C. B., Boogert, A. C. A., & Tielens, A. G. G. M. 2004, ApJ, 151, 35

Gillett, F. C. & Forrest, W. J. 1973, ApJ, 179, 483

Gingold, R. A. & Monaghan, J. J. 1977, MNRAS, 181, 375

Goldflam, R., Kouri, D. J., & Green, S. 1977, J. Chem. Phys., 67, 4149

Goodman, A. A., Benson, P. J., Fuller, G. A., & Myers, P. C. 1993, ApJ, 406, 528

Hartmann, L., Calvet, N., Gullbring, E., & D'Alessio, P. 1998, ApJ, 495, 385

Hartmann, L. & Kenyon, S. J. 1985, ApJ, 299, 462

Hartmann, L. & Kenyon, S. J. 1987, ApJ, 312, 243

Hayashi, C. 1981, in Fundamental Problems in the Theory of Stellar Evolution, IAU Symposium 93, ed. D. Sugimoto, D. Q. Lamb, & D. N. Schramm (D. Reidel Publishing Co., Dordrecht), 113–126

Hennebelle, P. & Falgarone, E. 2012, A&A Rev., 20, 55

Hogerheijde, M. R. & van der Tak, F. F. S. 2000, A&A, 362, 697

Hogerheijde, M. R., van Dishoeck, E. F., Blake, G. A., & van Langevelde, H. J. 1998, ApJ, 502, 315

Hughes, A. M., Wilner, D. J., Andrews, S. M., Qi, C., & Hogerheijde, M. R. 2011, ApJ, 727, 85

Ivezic, Z. & Elitzur, M. 1997, MNRAS, 287, 799

Jørgensen, J. K., Schöier, F. L., & van Dishoeck, E. F. 2002, A&A, 389, 908

Jørgensen, J. K., van Dishoeck, E. F., Visser, R., et al. 2009, A&A, 507, 861

Jørgensen, J. K., Visser, R., Sakai, N., et al. 2013, ApJ, 779, L22

Kennicutt, R. C. & Evans, N. J. 2012, ARA&A, 50, 531

Kenyon, S. J., Calvet, N., & Hartmann, L. 1993, ApJ, 414, 676

Kenyon, S. J. & Hartmann, L. 1987, ApJ, 323, 714

Kenyon, S. J. & Hartmann, L. W. 1990, ApJ, 349, 197

Kristensen, L. E., van Dishoeck, E. F., Bergin, E. A., et al. 2012, A&A, 542, A8

Larson, R. B. 1969, MNRAS, 145, 271

Larson, R. B. 1972, MNRAS, 156, 437

Li, Z.-Y., Banerjee, R., Pudritz, R. E., et al. 2014, in Protostars and Planets VI, ed. H. Beuther, C. Dullemond, & T. Henning (Univ. of Arizona Press, Tucson), in press

Looney, L. W., Mundy, L. G., & Welch, W. J. 2003, ApJ, 592, 255

Lucy, L. B. 1977, AJ, 82, 1013

Luhman, K. L. 2012, ARA&A, 50, 65

Mac Low, M.-M. & Klessen, R. S. 2004, Reviews of Modern Physics, 76, 125

Matthews, B. C., Krivov, A. V., Wyatt, M. C., Bryden, G., & Eiroa, C. 2014, in Protostars and planets VI, ed. H. Beuther, C. Dullemond, & T. Henning (Univ. of Arizona Press, Tucson), in press

McKee, C. F. & Ostriker, E. C. 2007, ARA&A, 45, 565

McKee, C. F., Zweibel, E. G., Goodman, A. A., & Heiles, C. 1993, in Protostars and Planets III, ed. E. H. Levy & J. I. Lunine (Univ. of Arizona Press, Tucson), 327

Mestel, L. & Spitzer, Jr., L. 1956, MNRAS, 116, 503

Min, M., Dullemond, C. P., Dominik, C., de Koter, A., & Hovenier, J. W. 2009, A&A, 497, 155

Monaghan, J. J. 1992, ARA&A, 30, 543
Murillo, N. M., Lai, S.-P., Bruderer, S., Harsono, D., & van Dishoeck, E. F. 2013, A&A, 560, A103
Nakano, T. & Nakamura, T. 1978, PASJ, 30, 671
Neufeld, D. A. 2012, ApJ, 749, 125
Öberg, K. I., Boogert, A. C. A., Pontoppidan, K. M., et al. 2011, ApJ, 740, 109
Öberg, K. I., van Dishoeck, E. F., & Linnartz, H. 2009, A&A, 496, 281
O'Dell, C. R. & Wen, Z. 1994, ApJ, 436, 194
Ogino, S., Tomisaka, K., & Nakamura, F. 1999, PASJ, 51, 637
Oliveira, I., Olofsson, J., Pontoppidan, K. M., et al. 2011, ApJ, 734, 51
Oliveira, I., Pontoppidan, K. M., Merín, B., et al. 2010, ApJ, 714, 778
Ossenkopf, V. & Henning, T. 1994, A&A, 291, 943
Pinto, R. F., Brun, A. S., Jouve, L., & Grappin, R. 2011, ApJ, 737, 72
Pollack, J. B., Hubickyj, O., Bodenheimer, P., et al. 1996, Icarus, 124, 62
Robitaille, T. P. 2011, A&A, 536, A79
Robitaille, T. P., Whitney, B. A., Indebetouw, R., Wood, K., & Denzmore, P. 2006, ApJ, 167, 256
Ros, K. & Johansen, A. 2013, A&A, 552, A137
Roueff, E. & Lique, F. 2013, Chemical Reviews, 113, 8906
Safronov, V. S. 1969, Evoliutsiia doplanetnogo oblaka.
Sargent, A. I. & Beckwith, S. 1987, ApJ, 323, 294
Schneider, N., Csengeri, T., Hennemann, M., et al. 2012, A&A, 540, L11
Schöier, F. L., van der Tak, F. F. S., van Dishoeck, E. F., & Black, J. H. 2005, A&A, 432, 369
Shakura, N. I. & Sunyaev, R. A. 1973, A&A, 24, 337
Shu, F. H. 1977, ApJ, 214, 488
Springel, V. 2005, MNRAS, 364, 1105
Springel, V. 2010, ARA&A, 48, 391
Steinacker, J., Baes, M., & Gordon, K. D. 2013, ARA&A, 51, 63
Stevenson, D. J. & Lunine, J. I. 1988, Icarus, 75, 146
Stone, J. M. & Norman, M. L. 1992, ApJ, 80, 753
Strom, K. M., Strom, S. E., Edwards, S., Cabrit, S., & Skrutskie, M. F. 1989, AJ, 97, 1451
Tasker, E. J., Brunino, R., Mitchell, N. L., et al. 2008, MNRAS, 390, 1267
Terebey, S., Shu, F. H., & Cassen, P. 1984, ApJ, 286, 529
Tielens, A. G. G. M. 2005, The Physics and Chemistry of the Interstellar Medium (Cambridge Univ. Press, Cambridge)
Tielens, A. G. G. M. 2013, Reviews of Modern Physics, 85, 1021
Tobin, J. J., Hartmann, L., Chiang, H.-F., et al. 2012, Nature, 492, 83
Ulrich, R. K. 1976, ApJ, 210, 377
van der Tak, F. 2011, in IAU Symposium 280, ed. J. Cernicharo & R. Bachiller (Cambridge Univ. Press, Cambridge), 449–460
van der Tak, F. F. S., Black, J. H., Schöier, F. L., Jansen, D. J., & van Dishoeck, E. F. 2007, A&A, 468, 627
van Dishoeck, E. F., Jonkheid, B., & van Hemert, M. C. 2006, Faraday Discussions, 133, 231
van Dishoeck, E. F., Kristensen, L. E., Benz, A. O., et al. 2011, PASP, 123, 138
van Leer, B. 1979, Journal of Computational Physics, 32, 101
Visser, R. & Bergin, E. A. 2012, ApJ, 754, L18
Visser, R., Kristensen, L. E., Bruderer, S., et al. 2012, A&A, 537, 55
Visser, R., van Dishoeck, E. F., Doty, S. D., & Dullemond, C. P. 2009, A&A, 495, 881
Vorobyov, E. I., Zakhozhay, O. V., & Dunham, M. M. 2013, MNRAS, 433, 3256
Whitney, B. A. & Hartmann, L. 1993, ApJ, 402, 605
Williams, J. P. & Cieza, L. A. 2011, ARA&A, 49, 67
Woodward, P. & Colella, P. 1984, Journal of Computational Physics, 54, 115
Woodward, P. R. 1978, ARA&A, 16, 555
Wyatt, M. C. 2008, ARA&A, 46, 339
Yang, B., Stancil, P. C., Balakrishnan, N., & Forrey, R. C. 2010, ApJ, 718, 1062
Yen, H.-W., Takakuwa, S., Ohashi, N., & Ho, P. T. P. 2013, ApJ, 772, 22
Yıldız, U. A., Kristensen, L. E., van Dishoeck, E. F., et al. 2013, A&A, 556, A89
Young, C. H. & Evans, II, N. J. 2005, ApJ, 627, 293
Zweibel, E. G. 1988, ApJ, 329, 384